Electronic Supplementary Material (ESI) for Journal of Materials Chemistry A.
This journal is © The Royal Society of Chemistry 2022

Electronic supplementary information

Plasmonic platinum nanoparticles—tungsten oxides nanoarchitectures as visible light photocatalysts for highly efficient overall water splitting

Leibo Gong, Qingyun Chu, Xinyu Liu, and Yiwei Tan*

State Key Laboratory of Materials-Oriented Chemical Engineering, School of Chemistry and Chemical Engineering, Nanjing Tech University, Nanjing 211816, China, Email: ytan@njtech.edu.cn

Experimental Section

Materials

Dihydrogen hexachloroplatinate(IV) hexahydrate ($H_2PtCl_6 \cdot 6H_2O$, 99.9%), sodium tungstate dihydrate ($Na_2WO_4 \cdot 2H_2O$, >99%), sodium borohydrate ($NaBH_4$, 98%), glacial acetic acid (>99%), isopropanol (99.5%), and ethanol (99.5%) were purchased from Alfa Aesar. L-Ascorbic acid (>99%), sodium citrate tribasic dihydrate (99%), and citric acid (99.5%) were commercially available from Sigma-Aldrich. All reagents were used without any further purification. Nickel foam (NF, 1.5-mm thickness) was purchased from Ailantian Advanced Technology Materials Co. Ltd.. A massive piece of NF was cut into equal parts (1 cm × 3 cm) and sequentially pretreated with isopropanol, hydrochloric acid (0.1 M), and anhydrous ethanol under ultrasonication to remove grease and the surface oxide layer. Ultrapure water (18.2 MΩ) produced with a Milli-Q purification system was used in the synthesis and photocatalytic measurements.

Characterization

Scanning electron microscopy (SEM) images were acquired using a Hitachi S-4800 field-emission scanning electron microscope operating at 5 kV to investigate the morphology of the photocatalysts. The XRD data were recorded using a Rigaku Smartlab diffractometer with Cu Kα radiation (λ = 1.5406 Å) operating at 40 kV and 100 mA at a scanning rate of 0.06^o sec^{-1}. The powder samples for XRD measurements were carefully scratched from the NF substrate and then deposited on clean glass slides. The Pt NPs in the redispersion (1 mg mL^{-1}) were deposited on clean glass slides for XRD measurements. Transmission electron microscopy (TEM) micrographs were obtained using a FEI Tecnai G2 Spirit Bio TWIN transmission electron microscope operating at an accelerating voltage of 120 kV. High resolution TEM (HRTEM) and scanning TEM (STEM) micrographs, high-angle annular dark field (HAADF)-STEM-energy-dispersive X-ray spectroscopy (EDX) elemental maps, and EDX spectra were acquired using a FEI ETEM Titan G2 60-300 Cs-corrected scanning transmission electron microscope equipped with a spherical aberration corrector for the electron beam and an energy-dispersive spectrometer (APOLLO XLT SDD system from EDAX) for chemical composition analysis operating at an accelerating voltage of 300 kV. STEM micrographs and EDX elemental maps were obtained in high-angle annular dark field (HAADF) mode. The specimens for TEM observations were carefully scratched from the NF substrate and sonicated before dropping them onto 300 mesh carbon-coated copper grids. UV-vis extinction spectra were recorded using a Shimadzu UV-3600 UV–vis–NIR spectrophotometer equipped with a LISR-3100 150 mm integrating sphere. The diffuse reflection spectra of all the samples were obtained using $BaSO_4$ as a standard reference in the measurements, where the fractional absorption was obtained according to the relationship of $A = 1 - (T + S)$, where A, T, and S denote absorption, transmission, and scattering, respectively. Nitrogen adsorption-desorption isotherm analysis was conducted by N_2 physisorption at 77 K using a BELSORP mini II apparatus (MicrotracBEL Inc.). The Brunauer–Emmett–Teller (BET) specific surface area (S_{BET}) and the pore size distribution (PSD) of the as-synthesized $WO_3 \cdot 0.5H_2O$–WO_3 and Pt—$WO_3 \cdot 0.5H_2O$–WO_3 specimens were achieved based on the corresponding N_2 adsorption isotherms in the relative pressure (P/P_0) range from 0.04 to 0.50 and the Barrett-Joyner-Halenda (BJH) method by using nitrogen adsorption data, respectively. The samples were degassed under high vacuum (< 0.01 mbar) at 150 °C for at least 6 h prior to the measurements. Thermogravimetry analysis was performed with a TGA7 thermogravimetric analyzer (Perkin-Elmer) under an argon atmosphere at a flow rate of 100 mL min^{-1}. Inductively coupled plasma optical emission spectrometry (ICP-OES, Prodigy, Leeman Labs Inc., λ = 165–800 nm, As = 200 nm) was also applied for determining the Pt mass loading after dissolving various composite photocatalysts in aqua regia. The samples were heated up to 900 °C at a temperature ramp of

10 °C min^{-1}. To evaluate the nature and onset of the electronic transitions, the band gap energies (Fig. 4(b) in the main text) are estimated by the equation:

$$\alpha hv = A_0(hv - E_g)^n \quad (1)$$

where α is the absorption coefficient and can be calculated by the equation:

$$\alpha = \frac{1}{D} log(\frac{1}{T + R}) \quad (2)$$

where *D*, *T*, and *R* are the material thickness, transmittance, and reflectance, respectively. *hv* is the photon energy in eV, and E_g is the band gap energy in eV. A_0 and *n* are constants and dependent on the type of electronic transition. The value of *n* is 1/2, 3/2, 2, or 3 for an allowed direct, a forbidden direct, an allowed indirect, or a forbidden indirect transition, respectively. According to eq 1, E_g of the samples can be determined by a linear plot of $(\alpha hv)^2$ versus energy *hv*. The intercept of the linear plot to the *x* axis yields the value of E_g for the samples. The VBM energy levels of various photocatalysts were determined by photo electron spectroscopy in air (PESA). The measurements were recorded using a Riken Keiki Model AC-2 PESA spectrometer with a power setting of 5 nW and a power number of 0.5. Photoluminescence (PL) emission spectra were recorded using a Horiba Scientific FluoroMax-4C-L spectrofluorometer. PL spectra were recorded on dry photocatalyst powders by using the following operating conditions: excitation wavelength at 300 nm; scanning speed of 200 nm min^{-1}; excitation slit width of 5 nm; emission slit width of 20 nm.

Photoelectrochemical (PEC) Measurements

PEC measurements were conducted in a three-electrode PEC cell with a platinum wire as the counter electrode in the dark and Ag/AgCl as the reference. The working electrode and the counter electrode are separately placed in a compartment separated by a glass frit containing nafion dispersions, allowing only protons to pass through. The working electrodes (photocathodes) were prepared by spreading slurries of $WO_3{\cdot}0.5H_2O{-}WO_3$ (dispersed in isopropanol (10 mg mL^{-1})) gently scratched from $WO_3{\cdot}0.5H_2O{-}WO_3$/NF obtained after hydrothermal reaction over 1 × 1 cm^2 FTO glass substrate to achieve a mass loading of 22.8 mg cm^{-2} and dried at 60 ºC overnight. Afterward, a dispersion of purified Pt130 NP solution (see the Experimental section in the text for the purification procedure) was evenly coated onto $WO_3{\cdot}0.5H_2O{-}WO_3$/FTO to obtain Pt130-3—$WO_3{\cdot}0.5H_2O{-}WO_3$/FTO (0.03 mg of Pt130 NPs per cm^2) and dried under vacuum at 60 ºC overnight. Pt130-3—$WO_3{\cdot}0.5H_2O{-}WO_3$/FTO and $WO_3{\cdot}0.5H_2O{-}WO_3$/FTO electrodes were calcined at 350 ºC in a horizontal tube furnace for 2h under N_2 flow (see the Experimental section in the text for the detailed procedure). An Ar-saturated aqueous solution of Na_2SO_4 (1 M) was used as an electrolyte. A 300 W xenon lamp (HSX–UV300) equipped with a cut-off filter L-42 or long pass filter LP 560 was used as light source for irradiating the active materials. To implement the PEC measurements, a copper wire was connected to the bare upper part of the FTO substrate of the working electrodes. There is a spacing of about 1 mm between the active material edge and the metal contact. A potentiostat (CHI660D, Chenhua, China) was employed to record the opencircuit voltage characteristics.

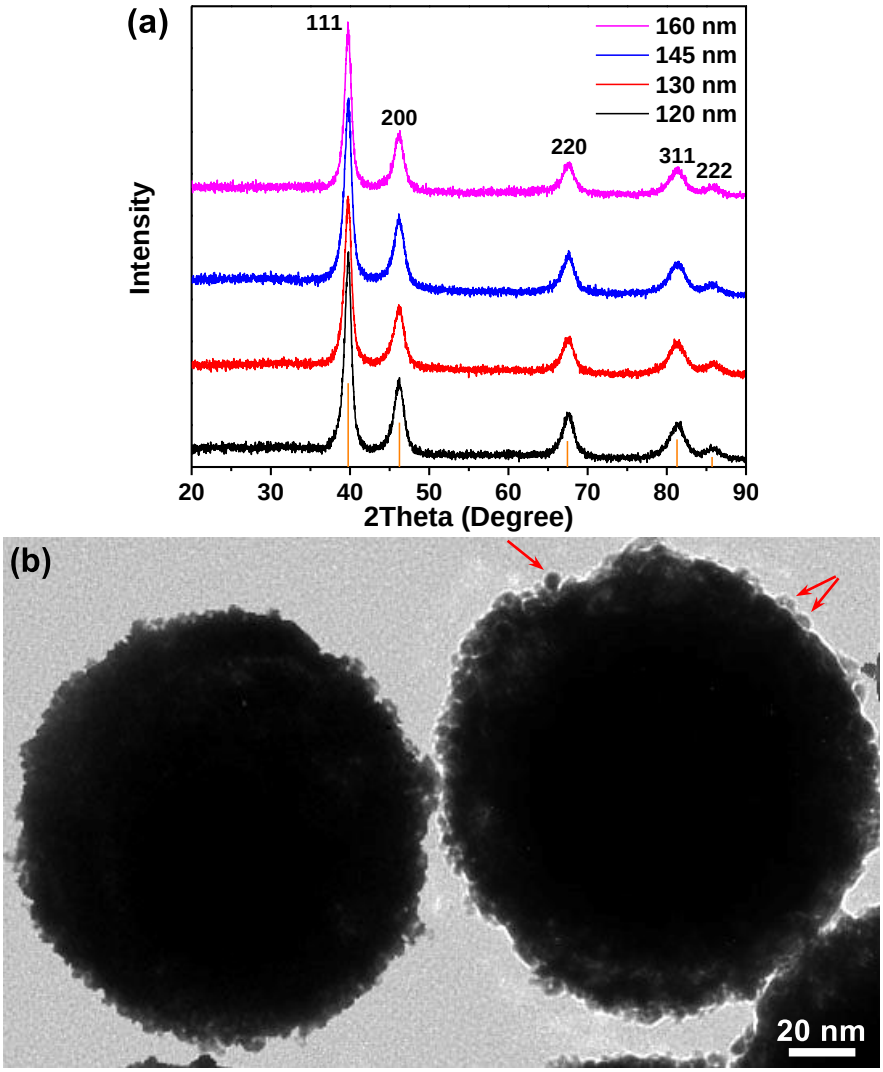

Figure S1. (a) XRD patterns of the monodisperse plasmonic Pt NPs with an average diameter of 120, 130, 145, and 160 nm. (b) TEM image of Pt NPs with an average diameter of 130 nm. The red arrows in part (b) indicate the crystallites bonded on the surface of Pt NPs.

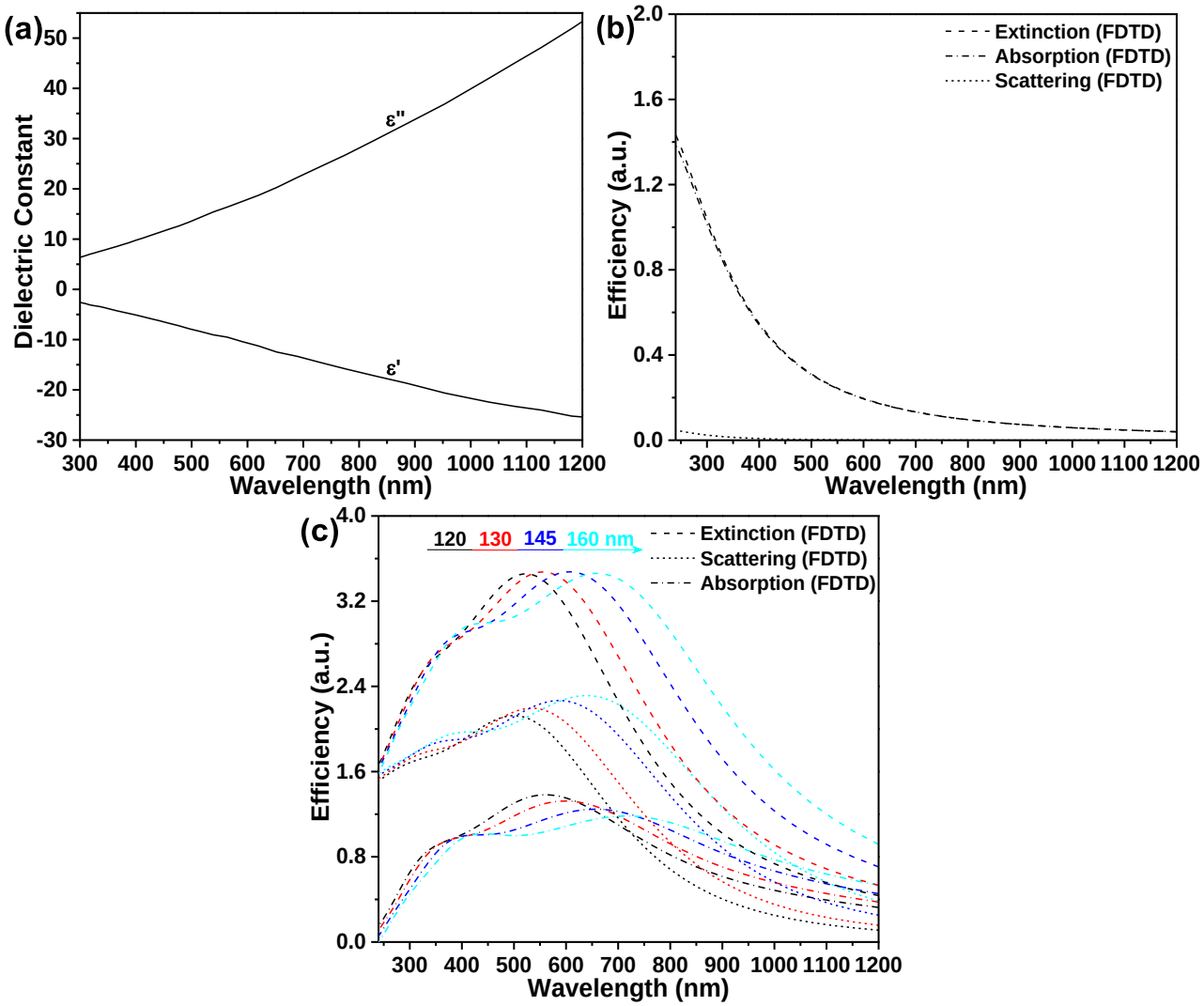

Figure S2. (a) Real (ε′) and imaginary (ε″) parts of the dielectric function of Pt metal shown as a function of wavelength. (b) Extinction (dash curve), absorption (dash dot curve), and scattering spectra (dot curves) of Pt nanoparticles with a diameter of 20 nm calculated using FDTD, showing the continuous spectral absorption arising from the dominant interband excitation (from the 4d band to 5s band) within the spectral range. (c) Calculated optical extinction (dash curves), scattering (dot curves), and absorption spectra (dash dot curves) of the Pt NPs with a diameter of 120, 130, 145, and 160 nm, where the interband contribution is minimum by the deduction of absorption efficiency value obtained in panel (b).

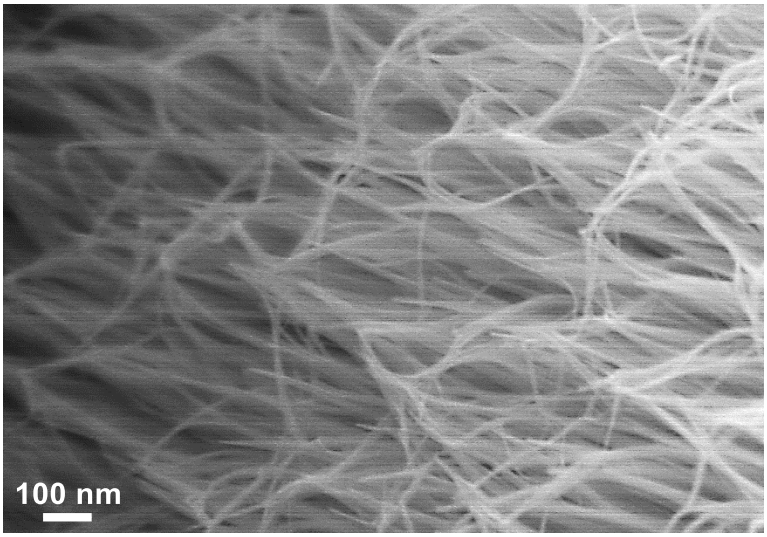

Figure S3. Zoom-in SEM image of the as-synthesized $WO_3 \cdot 0.5H_2O$–WO_3 nanowires grown on the fragments of $WO_3 \cdot 0.5H_2O$–WO_3 microplates.

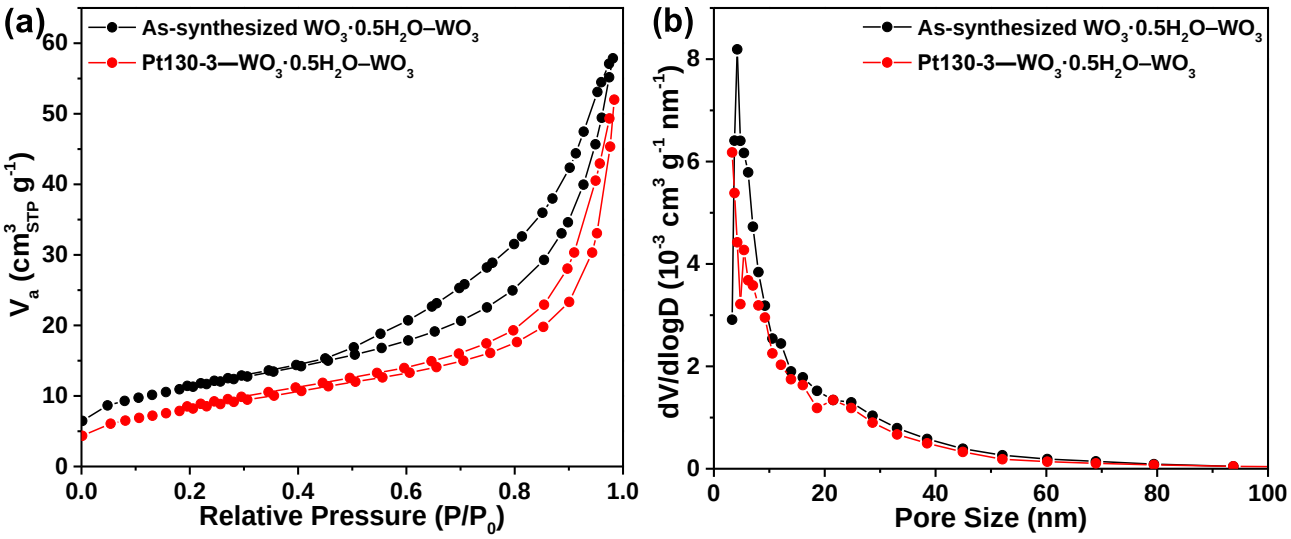

Figure S4. (a) N_2 (77.4 K) adsorption–desorption isotherms and (b) the corresponding BJH pore size distribution (PSD) plots of the as-prepared $WO_3 \cdot 0.5H_2O$–WO_3 hierarchical superstructures and Pt130-3—$WO_3 \cdot 0.5H_2O$–WO_3.

As shown in Figure S4a, the as-synthesized $WO_3 \cdot 0.5H_2O$–WO_3 and Pt130-3—$WO_3 \cdot 0.5H_2O$–WO_3 exhibit type IV nitrogen physisorption isotherms, which are characteristic for mesoporous materials with type H3 loops, resulting from wedge-shaped or slit-shaped pores. The occurrence of the dramatic adsorption hysteresis observed for both samples arises from capillary condensation in the overwhelming majority of mesopores and/or macropores. The PSD of the as-synthesized $WO_3 \cdot 0.5H_2O$–WO_3 sample shown in Figure S4b reveals a dominant peak of mesopores at *ca*. 4.0 nm and a shoulder peak of around 5.5 nm formed by the interspacing among $WO_3 \cdot 0.5H_2O$–WO_3 nanowires, as well as a weak peak of mesopores centered at *ca*. 25.0 nm formed by the interspacing among fragments of microplates. Similarly, we can also observe a dominant peak below *ca*. 3.0 nm, a moderate peak of around 5.5 nm, and a weak peak at *ca*. 21.5 nm for the Pt130-3—$WO_3 \cdot 0.5H_2O$–WO_3 sample. These results further verify the photocatalysts with rich porosity originating from excessively ample spacings in the 3D hierarchical $WO_3 \cdot 0.5H_2O$–WO_3 superstructures.

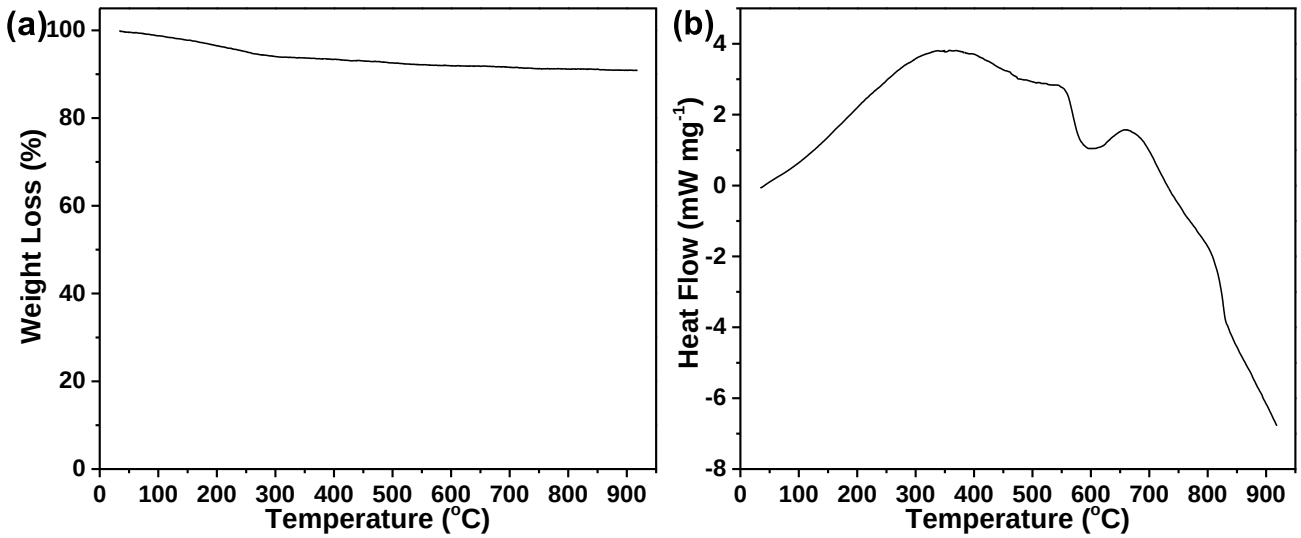

Figure S5. (a) Thermogravimetric curve and (b) DSC curve of the as-synthesized $WO_3 \cdot 0.5H_2O$–WO_3, showing the mass loss and phase transitions during thermolysis under Ar atmosphere.

Thermogravimetric analysis (TGA) was performed to detect the thermal stability of the as-synthesized $WO_3 \cdot 0.5H_2O$–WO_3 (Figure S5a). The evolution of water during the thermolysis shows a weight loss of 2.3% at ~155 °C related to the evaporation of the physically adsorbed water before this temperature. The following weight loss between 155 and 305 ºC is remarkable and reaches 6.0% which is associated with dehydration of tungsten oxide semihydrate to anhydrous tungsten oxide. A continuous weight loss up to 8.1% in the temperature range of 305 to 600 ºC indicates a gradually complete dehydration reaction of the $WO_3 \cdot 0.5H_2O$ component with an increase in temperature. Furthermore, there is a slight weight loss of 1.0% when increasing temperature from 600 to 900 ºC, which can be attributed to the thermally induced loss of lattice O^{2-} in WO_3 to form substoichiometric WO_{3-x} *via* O_2 gas evolution with increasing pyrolysis temperature. Accordingly, the weight ratio of $WO_3 \cdot 0.5H_2O$ in the as-synthesized $WO_3 \cdot 0.5H_2O$–WO_3 is calculated to be 77.5%.

Thermal transitions of the $WO_3 \cdot 0.5H_2O$–WO_3 during thermolysis is investigated by differential scanning calorimetry (DSC), as shown in Figure S5b. The DSC curve of the as-synthesized $WO_3 \cdot 0.5H_2O$–WO_3 shows a wide endothermic peak in the range of 100–550 ºC due to the dehydration of the sample. The endothermic peak maximum at *ca*. 350 °C is associated with the loss of constitutional water and indicates the maximum heat flow point for the dehydration of $WO_3 \cdot 0.5H_2O$. The local endothermic minimum around 600 ºC is associated with the complete decomposition of $WO_3 \cdot 0.5H_2O$ into WO_3. Concomitantly, a small endothermic peak at the higher temperature of *ca*. 660 ºC may be due to the phase transition/microstructural changes of tungsten oxides. With increasing the temperature to above 750 ºC, the exothermic crystallization of the WO_{3-x} occurs. It should be pointed out that the detailed studies on the structural and chemical changes of $WO_3 \cdot 0.5H_2O$–WO_3 at higher temperatures (> 500 ºC) are beyond the scope of this work and are left for future work.

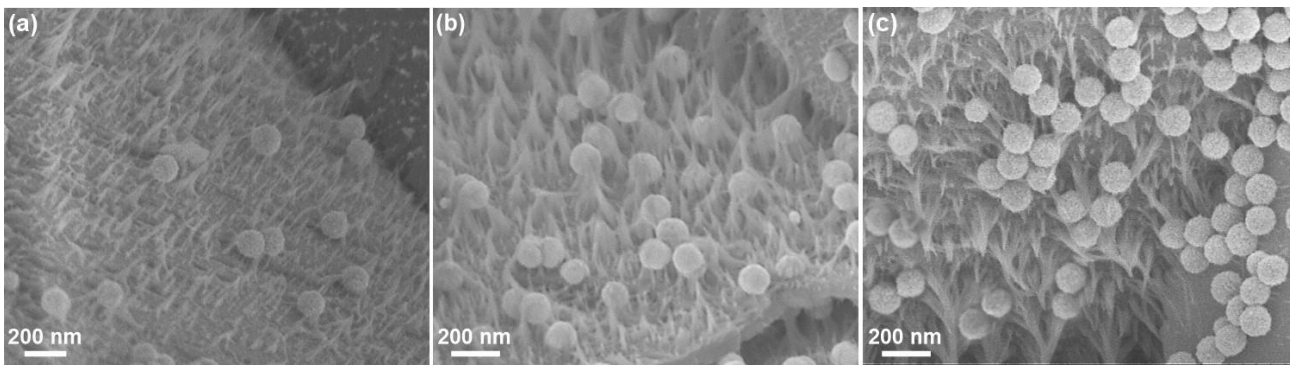

Figure S6. SEM images of (a) the Pt130-1—$WO_3 \cdot 0.5H_2O$–WO_3/NF, (b) Pt130-2—$WO_3 \cdot 0.5H_2O$–WO_3/NF, and (c) Pt130-4—$WO_3 \cdot 0.5H_2O$–WO_3/NF.

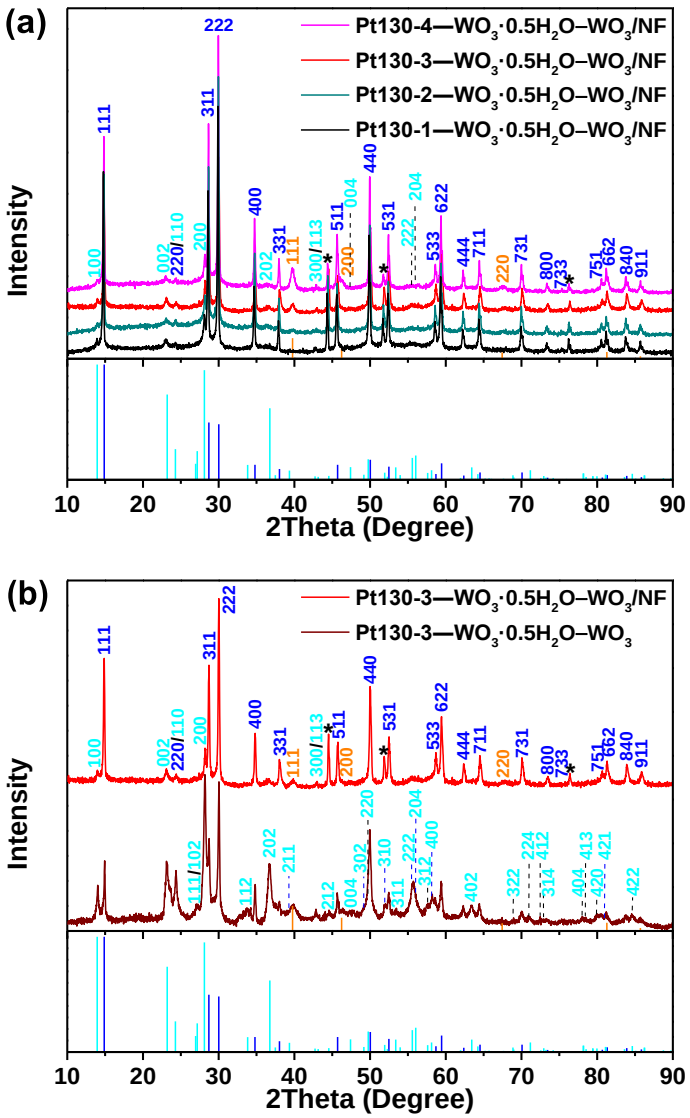

Figure S7. XRD patterns of (a) Pt130-*x*—$WO_3 \cdot 0.5H_2O$−WO_3/NF with a different areal mass loading of 130 nm Pt NPs and (b) Pt130-3—$WO_3 \cdot 0.5H_2O$−WO_3/NF and Pt130-3—$WO_3 \cdot 0.5H_2O$−WO_3 powders for comparison. The peaks marked by an asterisk arise from NF.

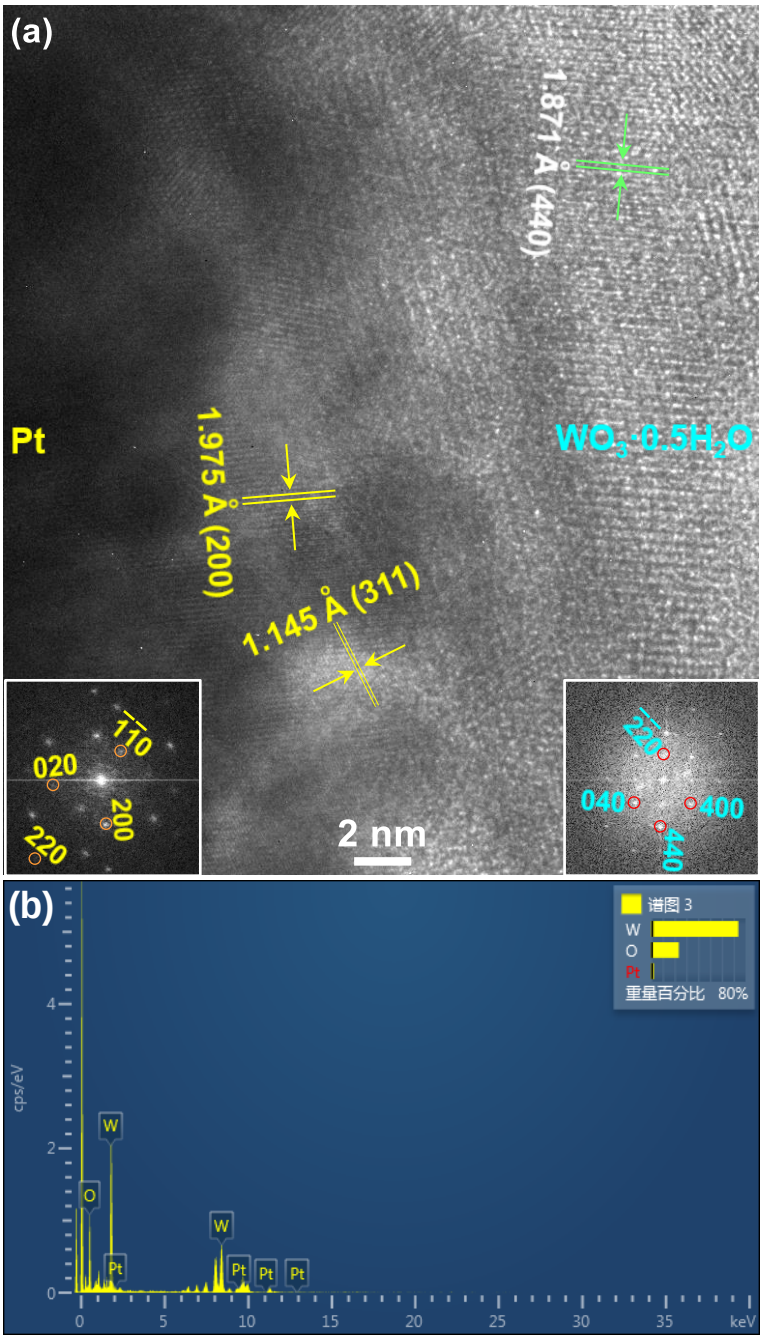

Figure S8. (a) HRTEM image and (b) EDX spectrum of the Pt130-3—$WO_3 \cdot 0.5H_2O$–WO_3. The HRTEM image in panel (a) is obtained at the interface region between Pt130 and $WO_3 \cdot 0.5H_2O$–WO_3.

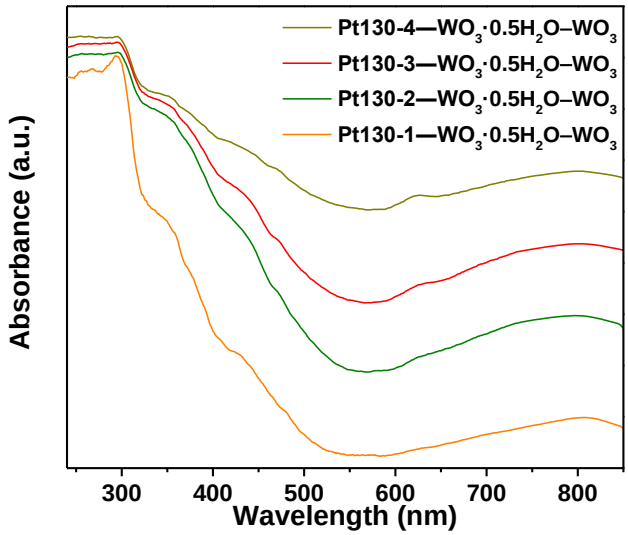

Figure S9. UV−vis diffuse reflectance spectra of the Pt130-*x*—WO_3·0.5H_2O−WO_3 with a different areal mass loading of Pt130 NPs.

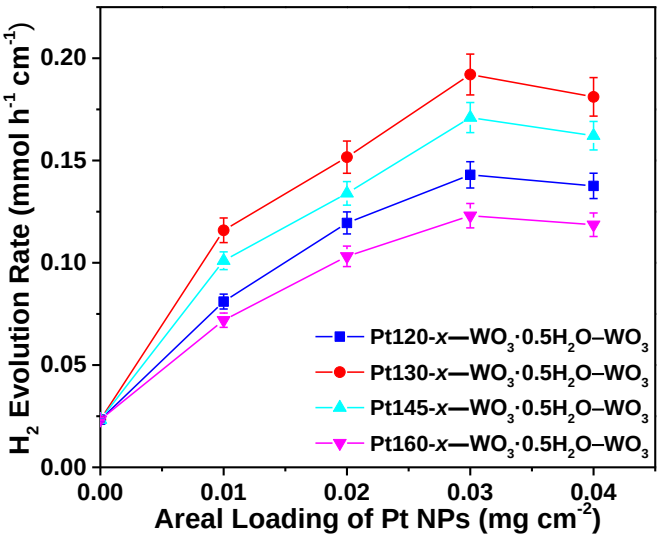

Figure S10. Average H_2 evolution rate over different Pt-*x*—WO_3·0.5H_2O−WO_3 (*x* = 1, 2, 3, and 4 representing for 0.01, 0.02, 0.03, or 0.04 in a unit of mg cm^{-2}) photocatalysts as a function of mass loading of Pt NPs. The data of each photocatalyst, including the error bar representing the standard deviation, are obtained from three parallelly prepared specimens.

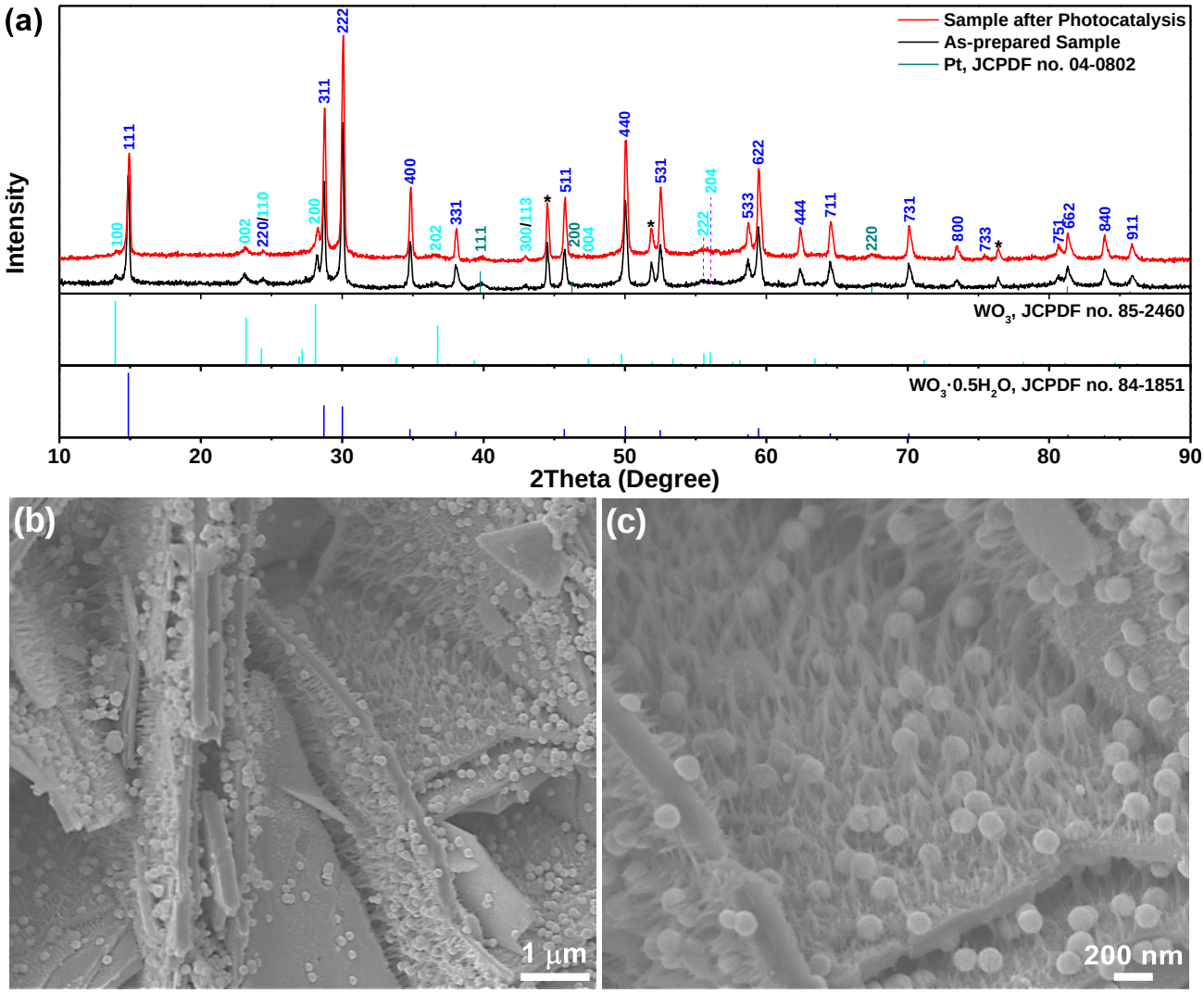

Figure S11. (a) Comparison of the XRD diffractograms of the as-prepared Pt130-3—$WO_3 \cdot 0.5H_2O$–WO_3 and this sample after three cycles of 8 h POWS. (b) Overview and (c) zoom-in SEM images of the Pt130-3—$WO_3 \cdot 0.5H_2O$–WO_3 after three cycles of 8 h POWS.

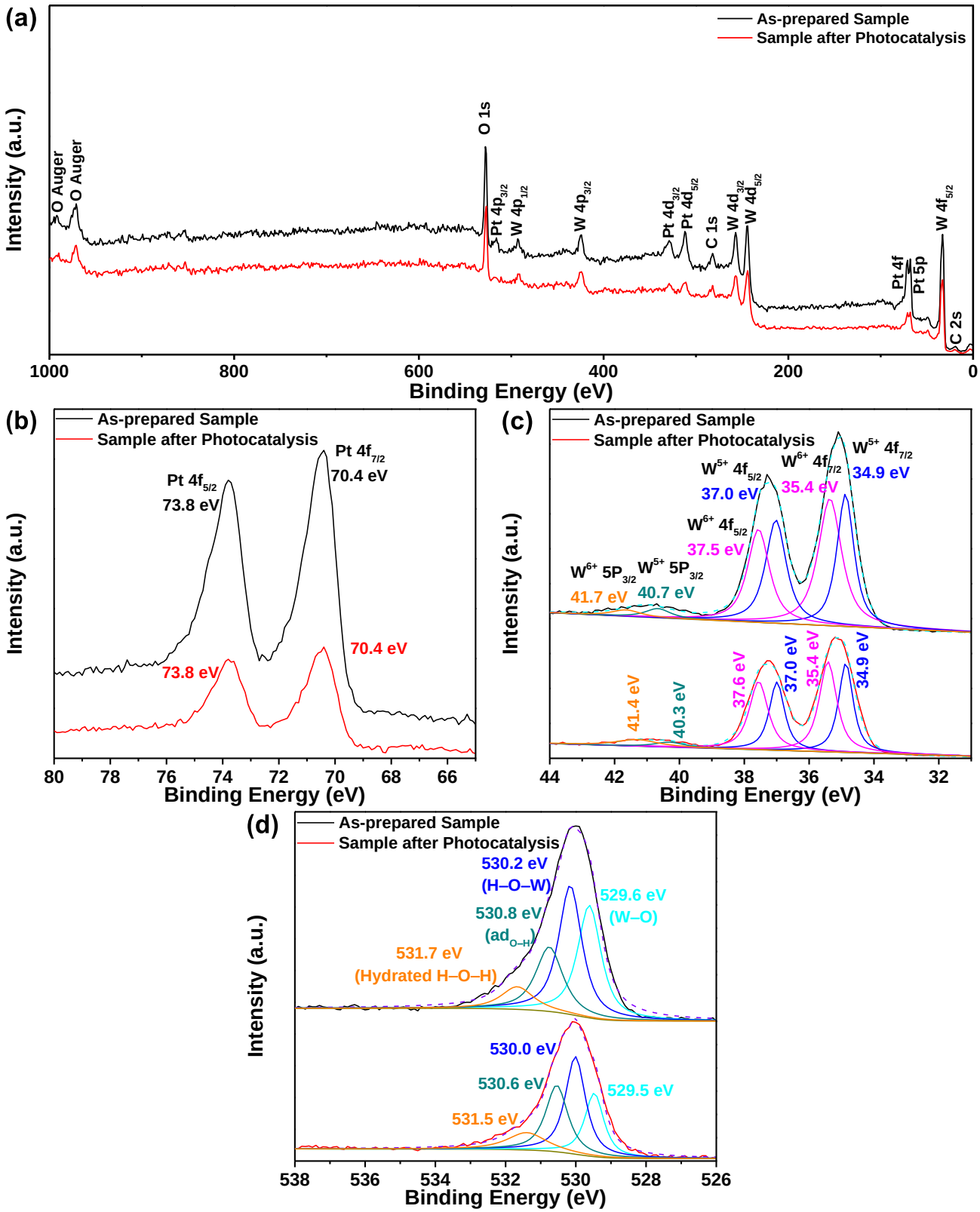

Figure S12. XPS spectra of the Pt130-3—$WO_3 \cdot 0.5H_2O$−WO_3 recorded before POWS reaction and after three cycles of 8 h POWS. (a) XPS survey spectra, (b) Pt 4f, (c) W 4f and 5p, and (d) O 1s core-level spectra.

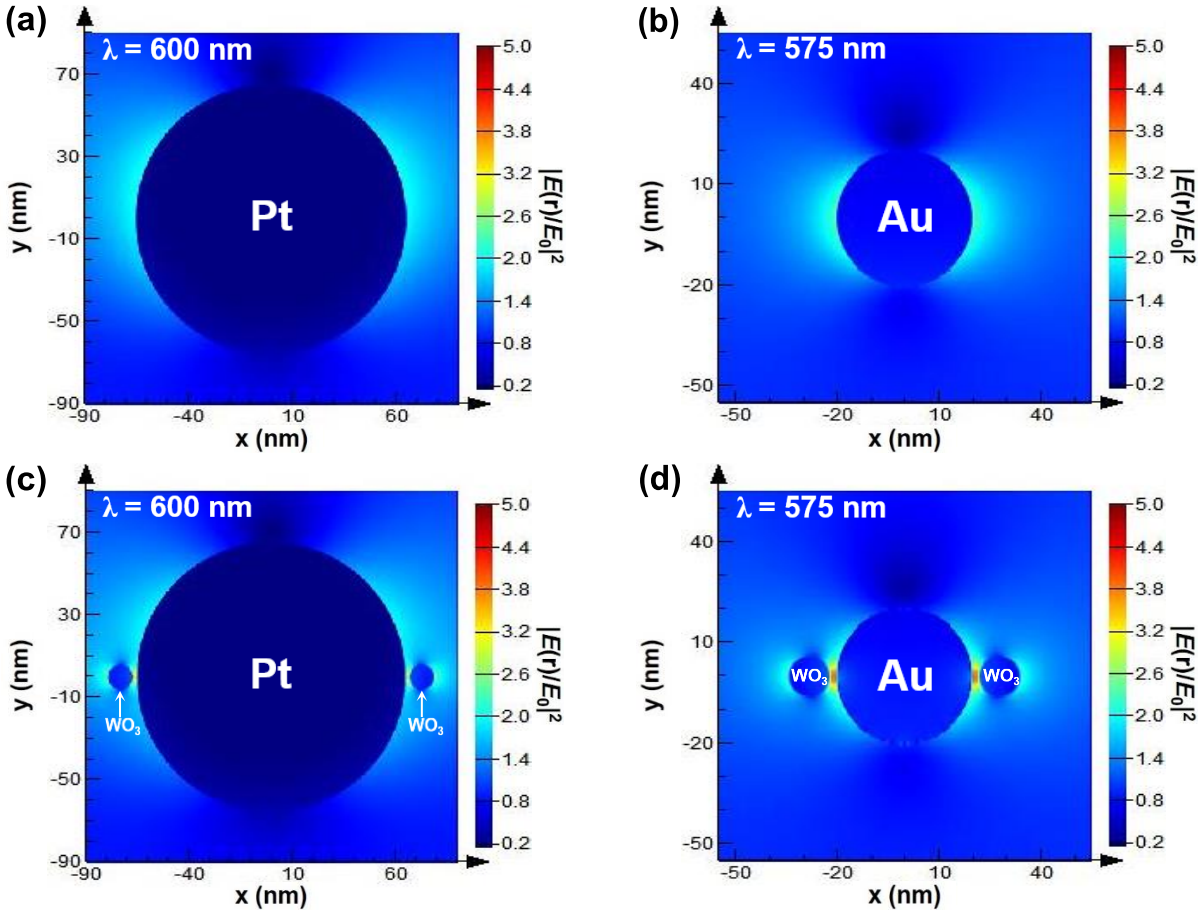

Figure S13. Comparison of plasmonic near-field distribution maps (cross-section view at z = 0) of (a) Pt130 nanospheres and (b) spherical Au NPs with a diameter of 40 nm (Au40) and electric field intensity enhancement contours of (c) the Pt130/WO_3 and (d) Au40/WO_3 hybrid systems under the parallel polarized excitation simulated using finite difference time domain methods, which show the evanescent electric near-field intensity enhancements $|E(r)/E_0|^2$ of the Pt and Au NPs at 600 and 575 nm, respectively. The color scale bar on the right side of each panel shows the relative increase in field enhancement. For simplicity, WO_3 NWs with a diameter of 5 nm are used to be representative for the $WO_3 \cdot 0.5H_2O$ NWs and $WO_3 \cdot 0.5H_2O$–WO_3 microplates. The geometrical shapes of the Pt130, Au40, and WO_3 NWs are established based on the TEM images. The corresponding optical-absorption maps in panels (a) and (b) illustrate that the Pt130 NPs exhibit a much weaker plasmonic near-field than the Au40 NPs.

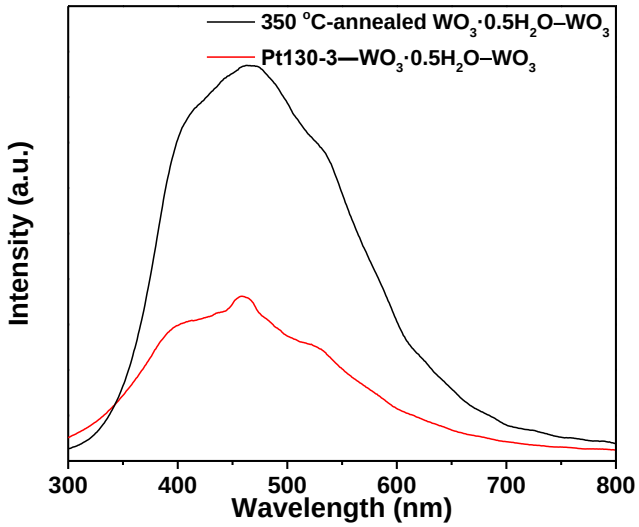

Figure S14. Photoluminescence spectra of Pt130-3—$WO_3 \cdot 0.5H_2O$–WO_3 and $WO_3 \cdot 0.5H_2O$–WO_3 at ambient temperature.

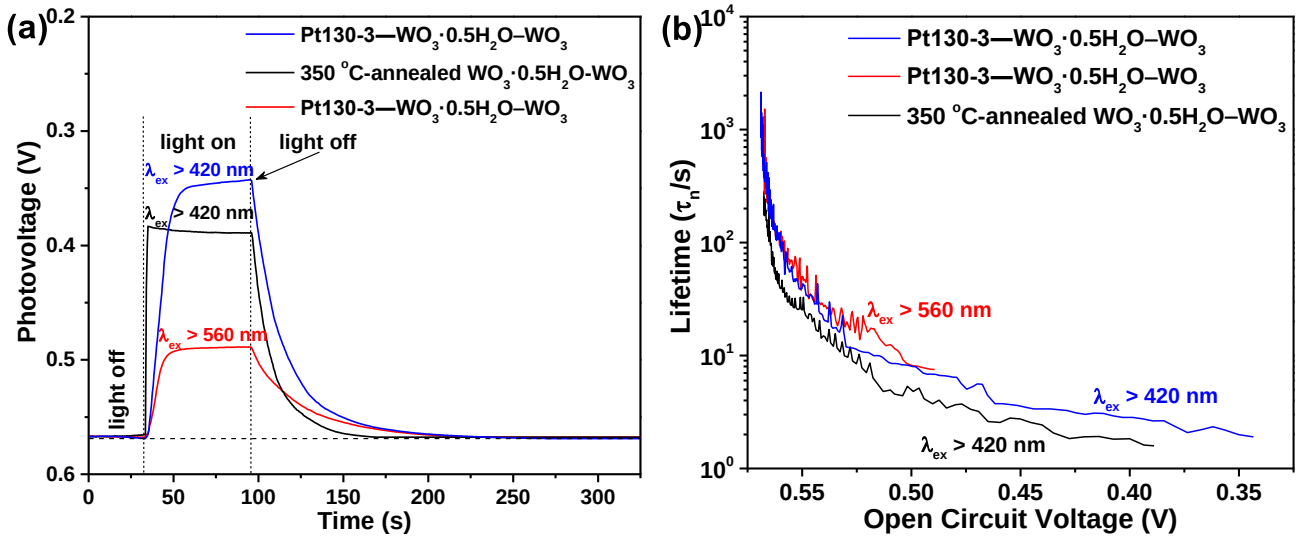

Figure S15. (a) Open circuit voltage (V_{OC})–time profiles under light on and off conditions and (b) average electron lifetime of Pt130-3—WO_3·0.5H_2O–WO_3 and 350 ºC-annealed WO_3·0.5H_2O–WO_3.

The V_{OC}–time profiles are recorded using a three-electrode photoelectrochemical (PEC) cell (see the Experimental Section) to probe the hot electron dynamics within the WO_3·0.5H_2O–WO_3 conduction band (CB) by exciting both the SPR and band gap transition of the Pt130-3—WO_3·0.5H_2O–WO_3 under λ_{ex} > 420 nm irradiation as well as the SPR of P130 NPs on the Pt130-3— WO_3·0.5H_2O–WO_3 under λ_{ex} > 560 nm irradiation, and by comparing them with the corresponding profile from the band gap transition of WO_3·0.5H_2O–WO_3 control sample (see Figure S15a). Upon light on, the V_{OC} decreases for the two photoelectrodes, arising from the accumulation of hot electrons (λ_{ex} > 560 nm, the red curve) or both hot and intrinsic bandgap transition electrons (λ_{ex} > 420 nm, the blue curve) within the CB of WO_3·0.5H_2O–WO_3 for the Pt130-3—WO_3·0.5H_2O–WO_3 or intrinsic bandgap transition for WO_3·0.5H_2O–WO_3 (λ_{ex} > 420 nm, the black curve). Note that compared to WO_3·0.5H_2O–WO_3, the gradual descending ramp of V_{OC} for the Pt130-3—WO_3·0.5H_2O–WO_3 is observed at the initial stage of irradiation, suggesting the limited transmission probability across the plasmonic metal–semiconductor interface. The Pt130-3—WO_3·0.5H_2O–WO_3 (the blue curve) exhibits a greater drop of V_{OC} than the WO_3·0.5H_2O–WO_3 (the black curve), presumably due to the efficient injection of hot electrons (besides bandgap transition electrons) into the WO_3·0.5H_2O–WO_3 CB under excitation with the shorter visible light. However, the Pt130-3—WO_3·0.5H_2O–WO_3 (the red curve) exhibits a smaller drop of V_{OC} under excitation with λ_{ex} > 560 nm than the WO_3·0.5H_2O–WO_3 with λ_{ex} > 420 nm, because of only hot electrons but without bandgap transition electrons injecting into the CB. Upon ceasing the illumination, the decay rates of V_{OC} for the Pt130-3—WO_3·0.5H_2O–WO_3 (the blue and red curves) are slower than that for the WO_3·0.5H_2O–WO_3 (the black curve). Furthermore, the lifetime of the photogenerated carriers (τ_n) at a different potential can be determined by the V_{OC} decay profile in Figure S15a and is plotted against V_{OC} in Figure S15b according to the following formula:[1,2]

$$\tau_n = -\frac{k_B T}{q}\left(\frac{dV_{OC}}{dt}\right)^{-1} \quad (3)$$

where τ_n is the average electron lifetime, k_B, T, and q are the Boltzmann constant, temperature, and charge of an electron, respectively. As can be seen, the hot electrons in the Pt130-3—WO_3·0.5H_2O–WO_3 exhibit a longer lifetime of ($\tau_n \approx 10^3$ s) than those in the WO_3·0.5H_2O–WO_3 ($\tau_n \approx 10^2$ s). Overall, the relatively long-lived distribution implying retarded recombination is observed for the hot electrons generated in Pt130-3—WO_3·0.5H_2O–WO_3 through the plasmon-mediated electron transfer process, especially evidenced by excitation with λ_{ex} > 560 nm. Meanwhile, the level of V_{OC} decrease for photoexciting the Pt130-3—WO_3·0.5H_2O–WO_3 with λ_{ex} > 420 nm, caused by concurrently photoexcited hot and intrinsic bandgap transition electrons in CB, appears to be smaller than the summation of those for photoexciting the Pt130-3—WO_3·0.5H_2O–WO_3 with λ_{ex} > 560 nm (caused by net hot electrons in the CB) and WO_3·0.5H_2O–WO_3 with λ_{ex} > 420 nm (caused by net bandgap transition electrons in the CB). This may be attributed for a portion of the photoexcited electrons from WO_3·0.5H_2O–WO_3 are neutralized by hot holes in plasmonic Pt NPs through hole tunneling or hole injection.

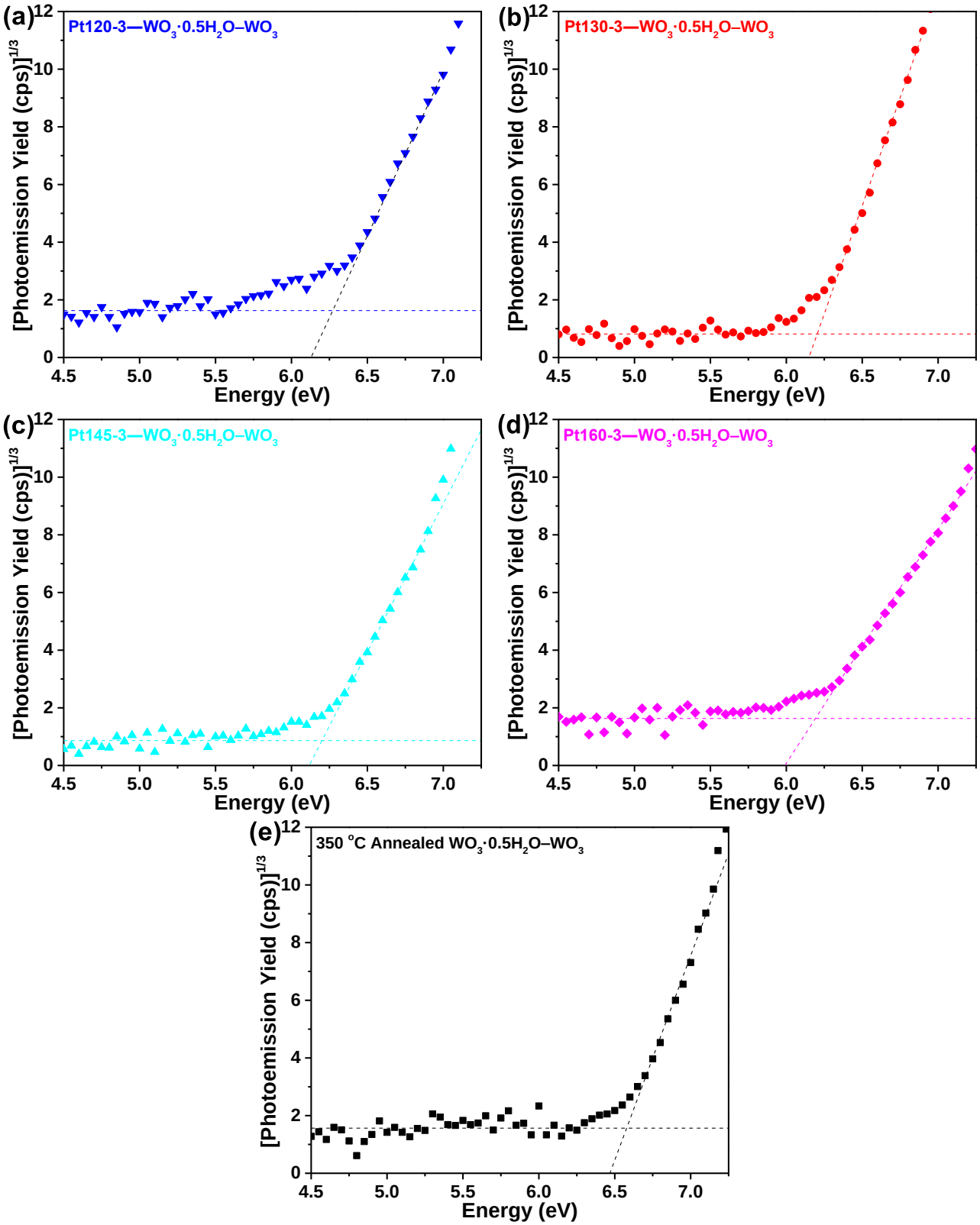

Figure S16. Photoelectron spectra in air for (a–d) various Pt-3—$WO_3 \cdot 0.5H_2O$–WO_3 and (e) the 350 ºC annealed $WO_3 \cdot 0.5H_2O$–WO_3 photocatalysts.

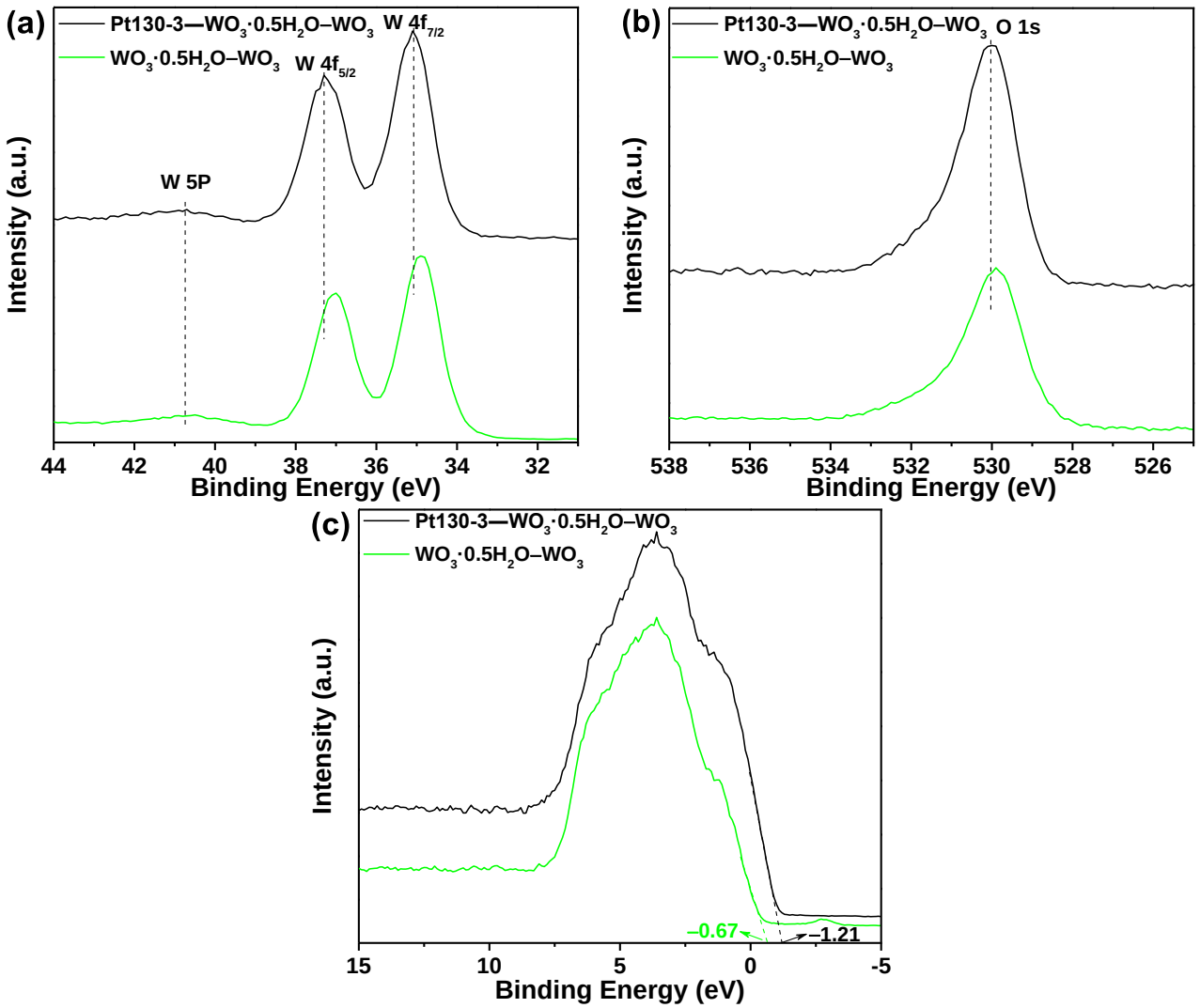

Figure S17. Comparison of XPS spectra of the Pt130-3—WO_3·0.5H_2O–WO_3 and WO_3·0.5H_2O–WO_3. (a) W 4f and 5p, (b) O 1s core-level spectra, and (c) valence band spectra.

Figure S17a and b show that the insignificant changes in W 4f, 5p, and O 1s binding energy (BE) values are found for Pt130-3—WO_3·0.5H_2O–WO_3 and WO_3·0.5H_2O–WO_3 within the XPS core-level spectrum resolution. Therefore, electron transfer is not expected to occur notably between Pt and WO_3·0.5H_2O–WO_3 constituents in the composite photocatalysts. However, note that the valence band (VB) spectrum of the Pt130-3—WO_3·0.5H_2O–WO_3 in Figure 17c is dramatically broadened, its low BE moieties account for a larger population in the VB regime, and its VB edge moves upward considerably (i.e., a shift to lower binding energy by 0.54 eV, which is close to relative shift of the VBM between Pt130-3—WO_3·0.5H_2O–WO_3 and WO_3·0.5H_2O–WO_3 derived from the PESA in Figure S16) compared to that of WO_3·0.5H_2O–WO_3, indicating the formation of new electronic states above the Fermi level by virtue of hybridization of the Pt d states and the neighboring W d states. Accordingly, the d band filling above the Fermi level is higher for the Pt130-3—WO_3·0.5H_2O–WO_3 than that for the WO_3·0.5H_2O–WO_3, giving rise to upward movement of the Pt—WO_3·0.5H_2O–WO_3 CBM.

Table S1. The designated and measured contents of Pt NPs in each Pt—$WO_3 \cdot 0.5H_2O$–WO_3 photocatalyst.

Photocatalyst	Designated content (wt%)	EDX content (wt%)	ICP-OES content (wt%)
Pt130-1—$WO_3 \cdot 0.5H_2O$–WO_3	0.044% (0.01 : 22.8 mg cm^{-2})	0.036%	0.042%
Pt130-2—$WO_3 \cdot 0.5H_2O$–WO_3	0.088% (0.02 : 22.8 mg cm^{-2})	0.095%	0.091%
Pt130-3—$WO_3 \cdot 0.5H_2O$–WO_3	0.13% (0.03 : 22.8 mg cm^{-2})	0.14%	0.13%
Pt130-4—$WO_3 \cdot 0.5H_2O$–WO_3	0.17% (0.04 : 22.8 mg cm^{-2})	0.19%	0.18%
Pt120-3—$WO_3 \cdot 0.5H_2O$–WO_3	0.13% (0.03 : 22.8 mg cm^{-2})	0.14%	0.12%
Pt145-3—$WO_3 \cdot 0.5H_2O$–WO_3	0.13% (0.03 : 22.8 mg cm^{-2})	0.15%	0.14%
Pt130-3—$WO_3 \cdot 0.5H_2O$–WO_3	0.13% (0.03 : 22.8 mg cm^{-2})	0.13%	0.14%

Table S2. Comparison of the rates of H_2 evolution (r_{H2}) and O_2 evolution (r_{O2}) over a different photocatalyst in pure water under visible-light irradiation (≥ 420 nm) obtained from a Xe lamp (300 W)[a]

Photocatalyst	r_{H2} (mmol h^{-1} cm^{-2})	r_{O2} (mmol h^{-1} cm^{-2})
Pt120-1—$WO_3 \cdot 0.5H_2O$–WO_3	0.0810	0.0399
Pt120-2—$WO_3 \cdot 0.5H_2O$–WO_3	0.119	0.0601
Pt120-3—$WO_3 \cdot 0.5H_2O$–WO_3	0.143	0.0720
Pt120-4—$WO_3 \cdot 0.5H_2O$–WO_3	0.138	0.0692
Pt130-1—$WO_3 \cdot 0.5H_2O$–WO_3	0.121	0.0596
Pt130-2—$WO_3 \cdot 0.5H_2O$–WO_3	0.153	0.0767
Pt130-3—$WO_3 \cdot 0.5H_2O$–WO_3	0.192	0.0954
Pt130-4—$WO_3 \cdot 0.5H_2O$–WO_3	0.181	0.0912
Pt145-1—$WO_3 \cdot 0.5H_2O$–WO_3	0.101	0.0509
Pt145-2—$WO_3 \cdot 0.5H_2O$–WO_3	0.134	0.0666
Pt145-3—$WO_3 \cdot 0.5H_2O$–WO_3	0.171	0.0857
Pt145-4—$WO_3 \cdot 0.5H_2O$–WO_3	0.162	0.0804
Pt160-1—$WO_3 \cdot 0.5H_2O$–WO_3	0.0719	0.0356
Pt160-2—$WO_3 \cdot 0.5H_2O$–WO_3	0.103	0.0519
Pt160-3—$WO_3 \cdot 0.5H_2O$–WO_3	0.123	0.0619
Pt160-4—$WO_3 \cdot 0.5H_2O$–WO_3	0.119	0.0597
Pt29-3—$WO_3 \cdot 0.5H_2O$–WO_3	0.0389	0.0196
$WO_3 \cdot 0.5H_2O$–WO_3	0.0233	0.0117
Pt120, Pt130, Pt145, and Pt160	0	0

[a] The values are obtained by averaging the data from three cycles (8 h/cycle).

Table S3. Comparison of the AQE obtained on various photocatalysts for water splitting under visible-light irradiation.

Photocatalyst	Irradiation wavelength	AQE	ref
Pt/Au/WO_3	λ = 550 nm	0.40%	21
$Pt_{0.5}$–Au_1/TiO_2	λ > 400 nm	0.8%	25
Rh/Cr_2O_3/Ta_3N_5/$KTaO_3$	λ = 420 nm	0.22%	48
Cr_2O_3/Rh/IrO_2–$Y_2Ti_2O_5S_2$	λ = 420 nm	0.36%	49
Au/CoO_x-$BiVO_4$–$Rh_yCr_{2-y}O_3$-ZrO_2/TaON	λ = 420 nm	10.3%	50
Pt/$Zn_{0.75}Cd_{0.25}Se$	λ = 400 nm	<0.1%	*ACS Catal*., 2021, **11**, 8004−8014
Ni-Ru/ZnSe:CGSe	λ = 420 nm	13.7%	*Chem. Sci*., 2020, **11**, 6436–6441
Au/TiO_2–Pt	λ = 550 nm	1%	*ACS Catal*., 2013, **3**, 1886–1891
Au-TiO_2	λ = 560 nm	7.5%	*J. Am. Chem. Soc*., 2011, **133**, 595–602

References

1. Bang, J.H.; Kamat, P.V. Solar Cells by Design: Photoelectrochemistry of TiO_2 Nanorod Arrays Decorated with CdSe. *Adv. Funct. Mater*. **2010**, *20 (12)*, 1970–1976.
2. Wang, X.; Pang, L.; Hu, X.; Han N. Fabrication of Ion Doped WO_3 Photocatalysts through Bulk and Surface Doping. *J. Environ. Sci*. **2015**, *35*, 76–82.